Long-Term Effects of Radiation Therapy on Cerebral Microvessel Proteome: A Six-Month Post-Exposure Analysis

Vikram Subramanian [1], Denise Juhr [1], Piero Giansanti [2], Isabella M. Grumbach [1,3,4*]

[1] Abboud Cardiovascular Research Center, Department of Internal Medicine, Carver College of Medicine, University of Iowa

[2] Bavarian Center for Biomolecular Mass Spectrometry at Klinikum rechts der Isar (BayBioMS@MRI), Technical University of Munich, Munich, Germany

[3] Free Radical and Radiation Biology Program, Department of Radiation Oncology, Carver College of Medicine, University of Iowa

[4] Iowa City VA Healthcare System, Iowa City, IA

Short title: RT-induced changes in mouse cerebral microvasculature

Word count:

* Corresponding author:
Isabella Grumbach, MD, PhD
University of Iowa
Carver College of Medicine
Division of Cardiovascular Medicine
4336 PBDB
169 Newton Road
Iowa City, IA, 52242
Phone: 319-384-4610
e-mail: isabella-grumbach@uiowa.edu

ABSTRACT

Background: Radiation therapy (RT) treats primary and metastatic brain tumors, with about one million Americans surviving beyond six months post-treatment. However, up to 90% of survivors experience RT-induced cognitive impairment. Emerging evidence links cognitive decline to RT-induced endothelial dysfunction in brain microvessels, yet *in vivo* studies of endothelial injury remain limited. Investigating the molecular and cellular pathways connecting RT, endothelial dysfunction, and cognitive impairment is vital for developing targeted interventions. This study examines proteomic changes in cerebral microvessels following RT.

Methods: We conducted a comprehensive quantitative analysis comparing the proteome in cerebral microvessels from five control mice and five irradiated mice (12 Gy) 6 months after RT. Bioinformatics analyses included gene ontology (GO) enrichment, Mitocarta analysis, Ingenuity Pathway Analysis (IPA), and iPathwayGuide. Predictions from the analyses were validated by western blotting.

Results: Our data identified significant dysregulation of 414 proteins following RT, with 157 upregulated and 257 downregulated. Gene ontology analysis indicated that the majority of the dysregulated proteins were part of various metabolic pathways. Cross referencing with Mitocarta revealed a significant presence of mitochondrial proteins among the dysregulated proteins, indicating potential mitochondrial metabolic dysfunction. Further investigation with IPA analysis uncovered 76 enriched canonical pathways, 34 transcription regulators, 6 nuclear receptors, and 5 growth factors involved in RT-induced damage responses in cerebral microvessels. IPA canonical pathway analysis predicted mitochondrial dysfunction due to inhibition of various metabolic pathways in the irradiated group. Validation with western blotting confirmed the bioinformatics predictions from the proteomic dataset.

Conclusions: Our data show significant proteomic changes in cerebral microvessels 6 months post-radiation, including oxidative phosphorylation, the TCA cycle, and glycolysis, suggesting metabolic mechanisms of RT-induced microvascular dysfunction.

2

Keywords: cerebral microvessels, proteomics, ingenuity pathway analysis, OXPHOS, TCA cycle and

Ubiquitin proteasome

1 INTRODUCTION

Microvascular injury is a hallmark of late radiation damage across various organs depending on the radiation field. Examples include renal dysfunction, skin fibrosis and heart failure [1-5]. One area where the effects of radiation on normal tissue are particularly apparent is injury after treatment of brain tumors [6-8]. In fact, up to 90% of patients experience cognitive function decline within three to six months after radiation [9-15]. Vascular damage, neuroinflammation and neuronal injury have been proposed as mechanisms driving cognitive decline [16]. Microvascular injury can compromise the blood-brain barrier (BBB) breakdown, leading to inflammatory cell infiltration and inflammation [17]. It can also result in apoptosis and senescence in vascular wall cells, potentially causing vascular rarefaction, reduced perfusion, and ischemia [18]. While there is consensus on a role of microvascular injury, the exact mechanisms and extent of microvascular injury's role in cognitive decline remains poorly understood.

In this study, we aimed to uncover changes in the microvascular proteome following RT. We chose to conduct our study using 12-month-old mice, approximately equivalent to 60-year-old humans, which is close to the reported median age of patients treated with radiation therapy for brain tumors [19]. Of note, there is age-dependent variation in brain radiation injury, with the highest pathology occurring in the very young and elderly [16,20]. We also opted for a six-month follow-up to focus on chronic changes from radiation injury. Previous work, including our own, has suggested that various pathways, such as mitochondrial injury, altered vascular transport, and changes in cell adhesion and tight junctions, may play a role in the long-term effects of radiation [21-25]. To gain an unbiased view on long-term effects of radiation exposure on the cerebral microvessel proteome, we conducted bioinformatics analyses using Ingenuity Pathway Analysis (IPA) and iPathwayGuide to identify significantly affected canonical pathways that may contribute to cerebral microvasculature dysfunction. Additionally, we performed immunoblotting to validate our proteomics findings and bioinformatics results.

2 MATERIALS AND METHODS

2.1 Animals Housing and Irradiation Procedure

One-year-old male C57BL/6J mice were obtained from the Jackson Laboratory. The mice were randomly assigned to the treatment (RT) or the control group, each with five animals. They were housed in temperature-controlled rooms with a 12-hour light/dark cycle, provided standard rodent chow, and had water access *ad libitum*. To avoid gender-related confounding factors, only male mice were used. The control group mice (n=5) underwent sham irradiation, anesthetized with ketamine and xylazine, placed in the radiation chamber without exposure. Mice were randomly selected for irradiation versus sham treatment. The irradiated group (n=5) received a 12 Gy X-ray dose to the whole brain using the XStrahl Small Animal Radiation Research Platform, which uses a 60 kVp beam of 0.2 mm Al quality for Cone Beam CT and a 220 kVp 0.63 mm Cu quality beam for treatment. The 12 Gy dose corresponds to 2 Gy fractions of a 40 Gy total, commonly used for RT in patients with five or more brain metastasis. Both groups were euthanized six months post-irradiation for analysis. No mice were excluded from the analysis. All experimental procedures were approved by the Institutional Animal Care and Use Committees of the University of Iowa and the Iowa City VA Health Care System, following Institute for Laboratory Animal Research standards.

2.2 Isolation of Cerebral Microvessels and Preparation of Protein Samples

Mice were euthanized using 100% CO_2 inhalation, followed by cervical dislocation. Brains from both control and irradiated groups were surgically removed, rinsed with cold Dulbecco's phosphate-buffered saline (DPBS) (Gibco #2430024), snap-frozen in liquid nitrogen, and stored at −80 °C. Cerebral microvessels were isolated following Lee et al [26]. Briefly, brain tissue was homogenized with a loose-fit Dounce grinder (Sigma-Aldrich #D9063) in MCDB 131 medium (Thermo Fisher Scientific #10372019) and centrifuged at 2,000 g for 15 minutes at 4 °C. The pellet was resuspended in a 15% (wt./vol) 70-kDa dextran solution (Sigma-Aldrich #31390) and centrifuged at 7,000 g for 15 minutes at 4 °C. The top layer containing myelin and parenchymal cells was discarded. Microvessels were collected using a 40-

µm cell strainer (Corning #352340), rinsed with cold DPBS, and transferred into MCDB 131 medium containing 0.5% (wt./vol) BSA (Millipore Sigma #126609). The suspension was centrifuged at 16,100 g for 30 minutes at 4 °C to pellet the microvessels. Pellets were stored at −80 °C for analysis.

For protein extraction, the isolated microvessel pellets were mixed with 130 µl of RIPA buffer (Fisher Scientific #R0278) containing protease (Pierce™ #A32963) and phosphatase inhibitor cocktails (Pierce™ #A32957). The mixture was vortexed three times for 30 seconds each (Fisher Scientific #0215370), then agitated for 30 minutes at 15-20 °C. Samples were vortexed again and heated at 95 °C for 10 minutes. To further break down the tissue, the samples were lysed using a Covaris E220 focused ultrasonicator (Covaris #500239) with following parameters. The instrument parameters for shearing were as follows: water level set point 10, water temperature 6°C, peak incident power 175 W, duty factor 10%, cycles per burst 200, and duration 300 s. Homogenized lysates were transferred to Eppendorf tubes and centrifuged at 16,100 g (Eppendorf #5415R) for 30 minutes. The supernatant was collected and stored at −80 °C. Total protein concentration was measured using a BCA protein assay kit (Pierce™ #23225). Finally, 30 µg of protein from each sample was used for quantitative proteomics analysis. Samples were labeled with a numeric identifier that did not include information about irradiation or sham treatment and sent for proteomic analysis.

2.3 Protein Digestion

Protein digestion was performed using the SP3 method [27]. For each sample, 30 µg of protein in 150 µL of lysis buffer was incubated with 10 µL of SP3 beads (a 1:1 mixture of Sera-Mag Speed Beads A and B, Thermo Scientific). Pure acetonitrile (ACN, VWR Chemicals) was added to a final concentration of 70% (v/v). The samples were incubated mixed at 800 rpm for 18 minutes, then placed on a magnet rack for 3 minutes to immobilize the SP3 beads. The supernatant was discarded, and the SP3 beads were washed three times with 1 mL of 80% ethanol/water (v/v) and once with 800 µL of ACN. Bound proteins were reduced with 100 µL of 10 mM 1,4-dithiothreitol (DTT, Sigma) in 50 mM ammonium bicarbonate (Sigma), pH 8.0, and incubated at 37 °C with shaking at 800 rpm for 1 hour. Proteins were

then alkylated with 55 mM 2-chloroacetamide (CAA, Sigma) for 1 hour at 37 °C in the dark. Finally, 1 µg of trypsin (Thermo Scientific) was added to each sample, and they were incubated overnight at 37 °C with shaking at 800 rpm. Digests were acidified with formic acid (FA, Carlo Erba) to a final concentration of 1% (v/v), dried in vacuo, and stored at −80 °C until use.

2.4 Automated Off-line Fractionation and LC-MS/MS Analysis

Peptides were re-suspended in 110 µL of buffer A (25 mM ammonium formate, pH 10) and subjected to high pH reverse-phase fractionation using the AssayMAP Bravo platform and 5 mL RP-S cartridges (Agilent). Cartridges were primed with 150 µL each of isopropanol, acetonitrile (ACN), and buffer B (80% ACN in 10 mM ammonium formate, pH 10) at a 50 µL/min flow rate. They were then equilibrated with 100 µL of buffer A, and peptides were loaded at 5 µL/min, collecting the flow-through (FT). Peptides were eluted with 25 mM ammonium formate, pH 10, using increasing ACN concentrations (5%, 10%, 15%, 20%, 25%, 30%, 80%). The seven fractions were pooled into four final fractions, dried in vacuo, and stored at −80 °C.

Nano-flow LC-MS/MS was performed using a Dionex Ultimate 3000 UHPLC+ system coupled to an Orbitrap Eclipse mass spectrometer (Thermo Fisher Scientific). Peptides were first delivered to a trap column (75 µm i.d. × 2 cm, packed in-house with 5 µm Reprosil C18 beads) and washed with 0.1% formic acid (FA) at 5 µL/min for 10 minutes, then transferred to an analytical column (75 µm i.d. × 45 cm, packed in-house with 3 µm Reprosil C18 beads) at 300 nL/min. Chromatographic separation used a linear gradient of solvent B (0.1% FA, 5% dimethyl sulfoxide (DMSO) in ACN) and solvent A (0.1% FA, 5% DMSO in water) over a 90-minute total run time.

Full-scan MS spectra were recorded in the Orbitrap from 360 to 1,300 m/z at 60,000 resolutions, with an automatic gain control (AGC) target of 100% and a maximum injection time (maxIT) of 50 ms. The most intense precursors were isolated with a 1.3 m/z isolation window for high-energy collisional dissociation (HCD) fragmentation. Fragment ions were recorded in the Orbitrap at 15,000 resolutions, with a maxIT of 22 ms and an AGC target of 200%. Normalized collision energy (NCE) was set to 25%.

7

Charge state screening selected precursors with charge states 2 to 6 for fragmentation, within a 2-second cycle time. Dynamic exclusion was set to 35 seconds.

2.5 Identification and Quantitation of Peptides and Proteins

Raw mass spectrometry data were processed using MaxQuant (version 2.2.0.0) with its built-in search engine, Andromeda [28]. Spectra were searched against the UniProtKB database for Mus musculus (UP000000589, 55,338 entries, downloaded October 2022). Enzyme specificity was set to trypsin, allowing up to two missed cleavages. The search included cysteine carbamidomethylation as a fixed modification, and protein N-term acetylation and methionine oxidation as variable modifications. Identifications were filtered to achieve a 1% false discovery rate (FDR) at protein and peptide levels. The "match between runs" and "second peptide" options were enabled. Label-Free Quantification (LFQ) was performed using the MaxLFQ algorithm [29]. The mass spectrometry proteomics data have been deposited in the ProteomeXchange Consortium via the PRIDE repository [30] with the dataset identifier PXD058732 (Website: http://www.ebi.ac.uk/pride, Username: reviewer_pxd058732@ebi.ac.uk, Password: RJJaEf7seviy).

2.6 Proteomics Data Analysis and Pathway Enrichment Analysis

Data analysis was performed using Maxquant and Perseus software (version 2.0.7.0). Protein identifications were filtered to remove contaminants and decoy hits before normalizing log2-transformed LFQ intensity values by median centering (Supplemental Table S1). Only proteins quantified in all biological replicates were retained for statistical analysis **(n = 2,457, Supplemental Table S2).** Significantly dysregulated proteins were identified using a Student's t-test with an S0 parameter of 0.1, with p-values adjusted using a permutation-based FDR of 5%. For the final quantifications, proteins identified by at least two unique peptides and demonstrating a fold change ratio of <0.77 or >1.30, with corrected p-values according to prior studies were defined as being significantly differentially expressed and used for all bioinformatics analysis **(n = 414, Supplemental Table S3)** [31-33]. Hierarchical cluster analysis of significantly dysregulated proteins was performed using SR plot [34]. A volcano plot illustrating

differentially expressed proteins was generated using VolcaNoseR [35]. Enrichment analysis of dysregulated proteins was conducted to assess their impact on biological processes, cellular locations, molecular functions, and KEGG pathways after radiation exposure, using HemI 2.0 [36]. Canonical pathway, upstream regulator and disease and biofunction analyses were performed with INGENUITY Pathway Analysis (IPA) software [37], applying a threshold of –log (p-value) >1.3. Pathways with a z-score >2.0 were considered activated, while those with a z-score <–2.0 were inhibited. Impact pathway analysis on differentially expressed proteins was conducted using iPathwayGuide [38] with pathway annotations from the KEGG database and gene ontology annotations from the Gene Ontology Consortium database. A threshold of FDR-corrected p-value <0.05 was used to identify significantly affected pathways.

2.7 Immunoblotting Analysis

Equal amounts of protein (10 µg) from control and irradiated groups were separated on NuPAGE 4% to 12% Bis-Tris gels (Life Technologies) and transferred to polyvinylidene difluoride (PVDF) membranes using the Mini-PROTEAN 3 blotting system (Bio-Rad). Membranes were stained with Ponceau S (Cell Signaling #59803S) to confirm protein transfer, washed in TBS with Tween™ (TBST), and blocked with 3% BSA (RPI Research #9048-46-8) or Starting Block™ Blocking Buffer (Thermo Fisher Scientific #37538) for 2 hours. Membranes were incubated overnight at 4°C with primary antibodies, including anti-NDUFB8 (Abcam, no. ab110413), anti-NDUFA11 (ABclonal, no. A16239), anti-NDUFA4 (ABclonal, no. A15693), anti-SDHA (Cell Signaling, no. 11998), anti-SDHB (Abcam, no. ab110413), anti-UQCRC2 (Aviva systems biology, no. OAAN01132), anti-MT-CO2 (ABclonal, no. A11154), anti-COX6B1 (ABclonal, no. A2228), anti-ATP5F1C (ABclonal, no. A15257), anti-ATP6VID (ABclonal, no. A12940), anti-ATP5F1A (ABclonal, no. A11217), anti-ACLY (ABclonal, no. A3719), anti-IDH3A (ABclonal, no. A14650), anti-DLD (ABclonal, no. A13296), anti-ACO2 (ABclonal, no. A3716), anti-MDH2 (ABclonal, no. A13516), anti-ENO2 (Cell Signaling, no. 9536), anti-TPI (ABclonal, no. A15733), anti-MPC1 (Cell Signaling, no.14462), and anti-MPC2 (Cell Signaling, no. 46141). After washing, membranes were

incubated with secondary antibodies at a 1:5000 dilution for 2 hours at room temperature. After washing, membranes were developed using the Cytiva Amersham™ ECL™ Prime Western Blotting Detection Reagent and scanned. Immunoblot bands from five biological replicates in both control and irradiated groups were analyzed and quantified using ImageJ software (http://rsbweb.nih.gov/ij/).

2.9 Statistical Analysis

All experiments were conducted in five biological replicates. Data were presented as mean with standard error, and statistical analyses were conducted using GraphPad Prism 9.0 software. Normal distribution was evaluated using the D'Agostino-Pearson omnibus normality test. Statistical significance for comparisons between two groups was determined using the non-parametric Mann-Whitney test. Differences were considered significant if p-values were <0.05.

3 RESULTS

3.1 Proteome profiling of cerebral microvessel after radiation therapy

To investigate the effects of radiation on cerebral microvasculature, we performed quantitative proteomics using LC-MS/MS on samples from mice six months after RT with 12 Gy x-ray or sham treatment **(Figure 1A)**. The full workflow for this proteomics study is shown in **Figure 1B**. A total of 7,462 proteins were detected, and 2,457 were quantified **(see Supplementary Table S1, S2)**. Label-free quantitation (LFQ) demonstrated reproducibility among biological replicates from both control and irradiated mice, as shown by Pearson correlation **(Figure 1C)**. Principal component analysis (PCA) using LFQ intensity values of all identified proteins revealed a clear separation between control and irradiated groups, indicating significant changes in protein expression due to radiation **(Figure 1D)**. Proteins were classified as identified with at least one valid MS/MS spectrum, quantified if detected in all five biological replicates, and dysregulated if their relative abundance significantly differed between the groups. Among the 2,457 quantified proteins, 414 proteins were significantly dysregulated between irradiated and control groups, and these proteins were used for further bioinformatics analysis. Hierarchical clustering of z-scored LFQ intensities of dysregulated proteins highlighted substantial expression differences between the groups **(Figure 2A)**. Of the 414 dysregulated proteins, 157 were upregulated, and 257 were downregulated **(see Supplementary Table S3)**. Volcano plots depicting these changes, with the top 10 proteins in each category labeled, are shown in **Figure 2B**.

To investigate the biological significance of the dysregulated proteins, we utilized the Helm webtool for further analysis. The highest representation of dysregulated proteins was observed in the cellular components "mitochondrion", "mitochondrial inner membrane", and "nuclear speck", a specialized subnuclear structure associated with splicing factors (**Figure 2C**). Regarding biological processes, proteins involved in mRNA splicing and processing, as well as the TCA cycle and mitochondrial respiratory chain complex I assembly, were predominantly affected (**Figure 2D**). For molecular function, dysregulated proteins were primarily associated with protein and RNA binding activities

11

(**Figure 2E**). A complete list of these categories and their corrected p-values is provided in **Supplementary Table S4**.

3.2 Impact Pathway Analysis

In addition, we analyzed all changes with iPathwayGuide that unlike other functional analysis tools, considers a gene's position within each pathway and its interactions with other genes. The analysis revealed that the significantly dysregulated proteins were enriched in 266 pathways, with strongest impact on metabolic pathways, nucleocytoplasmic transport, one carbon metabolism, oxidative phosphorylation, spliceosome, and the tricarboxylic acid cycle **(Figure 3A-F)**. Additionally, several non-metabolic pathways were significantly enriched in irradiated cerebral microvessels, including cGMP-PKG signaling, vascular smooth muscle contraction, mRNA surveillance, calcium signaling **(Supplemental Figure 1A-E)**, focal adhesion, tight junction, and gap junction, **(Supplemental Figure 2A-C)**. Moreover, proteins enriched in the spliceosome and mRNA surveillance pathways were upregulated in irradiated group, potentially suggesting an increased stress response and errors in mRNA processing due to radiation exposure. A complete list of enriched pathways and their corrected p-values is available in **Supplementary Table S5**.

The core analysis module in the Ingenuity Pathway Analysis (IPA) software was used to identify altered canonical pathways in cerebral microvessels following radiation therapy (RT). Using a -log (p-value) cutoff of 1.3 (Fisher's exact test) and a z-score threshold (Z-score > 2 for activation, Z-score < -2 for inhibition), 76 enriched canonical pathways were identified. Of these, 68 pathways were predicted to be inhibited and 8 activated post-RT. **Figure 4A-C** and **Supplementary Table S6** highlight 15 canonical pathways associated with cerebral microvessel function. Based on altered protein expression, the three most significantly inhibited pathways were oxidative phosphorylation, the TCA cycle, and Gαq signaling, while the five most significantly activated pathways included mitochondrial dysfunction, sirtuin signaling, granzyme A signaling, the spliceosomal cycle, and RHOGDI signaling.

12

An upstream regulator analysis using the z-score algorithm identified 34 enriched transcription regulators in irradiated cerebral microvessels. The top activated regulators were KDM5A (Z-score = 4.243), CLPB (Z-score = 3.742), HOXA10 (Z-score = 2.714), and RELA (Z-score = 2.201), while the top inhibited regulators included TEAD1 (Z-score = -4.899), PPARGC1A (Z-score = -4.872), RB1 (Z-score = -3.90), HNF1A (Z-score = -2.985), and MITF (Z-score = -2.887) (**Figure 4B**).

A disease and biofunction analysis of 414 differentially expressed proteins revealed enrichment for 41 diseases and biological functions post-radiation exposure. Of these, 31 functions were predicted to be inhibited, while 10 were activated. **Figure 4C** depicts the selected 10 enriched diseases/biological functions, associated molecules, and their p-values and z-scores. Notable affected functions in cerebral microvessels after radiation therapy included cell migration, cell-to-cell contact, ATP synthesis, molecule transport, and fatty acid metabolism, as detailed in **Supplementary Table S6**.

3.3 RT induces changes in the expression of mitochondrial proteins within Cerebral Microvessels.

Given the strong evidence for changes in the mitochondrial proteome by different analysis tools, we investigated the impact of RT on mitochondrial protein expression and associated functions in more detail. We mapped all 2,467 quantified cerebral microvessel proteins to the Mouse Mitocarta3.0 database. This analysis identified 385 mitochondrial proteins, with 84 significantly dysregulated (all downregulated) in the irradiated group compared to controls **(Figure 5A; Supplementary Table S7)**.

We created a hierarchical cluster heatmap using the LFQ intensity of significantly dysregulated mitochondrial proteins, clearly separating control and irradiated groups (**Figure 5B**). To confirm the biological significance of these changes and their impact on mitochondrial function, we performed gene ontology (GO) analysis with the Helm webtool. The most affected proteins were linked to the

13

mitochondrial inner membrane, mitochondrial respiratory chain complex I, and mitochondrial matrix (**Supplementary Figure 3A, Supplementary Table S8**). Key impacted biological processes included mitochondrial respiration, the tricarboxylic acid cycle, and 2-oxoglutarate metabolic process (**Supplementary Figure 3B**).

Using IPA core analysis, we examined affected canonical pathways in the mitochondrial protein data set. This analysis identified 14 enriched pathways, 10 predicted to be inhibited and 4 activated following radiation treatment. The top three inhibited pathways were oxidative phosphorylation, neutrophil extracellular trap signaling, and the TCA cycle (**Figure 5C**). Additionally, upstream regulator analysis for transcription factors associated with mitochondrial proteins identified 14 enriched regulators. Among those, CLPB, and HIF1A were the top activated regulators, while TEAD1, PPARGC1A, and RB1 were the most inhibited (**Figure 5D**). Supplementary Table S9 provides a comprehensive list of canonical pathways, upstream regulators, and associated p-values.

Lastly, we used IPA software to map altered diseases and biological functions based on dysregulated mitochondrial proteins. The analysis highlighted 22 enriched diseases and functions, 17 predicted to be inhibited and 5 activated. Notably, ATP synthesis and nucleic acid metabolism were predicted to decrease, while synthesis, production and metabolism of reactive oxygen species were predicted to increase (**Figure 5E**).

3.4 Metabolic pathways are affected in cerebral microvessels after RT.

Energy metabolism is essential for biosynthetic processes to facilitate the restoration of cell damage. While previous studies have extensively explored the impact of radiation on cardiac energy metabolism [31,39,40] and metabolic pathways in other tissues [41,42] the impact of radiation on cerebral microvessel metabolism is less understood. Our proteomic analysis revealed altered expression of proteins linked to key metabolic pathways, including oxidative phosphorylation (n=29), the TCA cycle (n=15), and

14

glycolysis (n=7) (**Supplementary Figure 4A-C**). IPA analysis suggested inhibition of oxidative phosphorylation, the TCA cycle, glycolysis, and gluconeogenesis. To confirm these findings, we used western blotting to analyze dysregulated proteins in oxidative phosphorylation, the TCA cycle, and glycolysis.

Our analysis revealed radiation-induced changes in the expression of proteins across various OXPHOS system complexes. Western blot images for different OXPHOS protein subunits with adjustment for loading by Ponceau-stained whole membranes revealed significant downregulation of complex I proteins NDUFA11 and NDUFB8 (**Figure 6A-C**), complex II protein SDHB (**Figure 6A-C**), and complex IV protein MT-CO2 (**Figure 6A-C**) in irradiated samples. Although downregulation of complex III and V proteins ATP5F1C, ATP6VID, and ATP5F1A was observed, these changes did not reach statistical significance (**Figure 6A-C**).

Lastly, we examined proteins involved in the TCA cycle, glycolysis, and pyruvate transport (**Supplemental Figure 5A**) and detected non-significant trends towards decreases for TCA cycle proteins UQCRC2, ACLY, ACO2, IDH3A, DLD, SDHA, and MDH2 in the irradiated group (**Supplemental Figure 5B**). Similarly, analysis of glycolysis and pyruvate transport proteins revealed similar trends for glycolytic proteins TPI and ENOL2 as well as mitochondrial pyruvate carrier proteins MPC1 and MPC2 in the irradiated group (**Supplemental Figure 5C, 5D**).

4 DISCUSSION

Our study provides the first in-depth analysis of long-term proteome changes in non-tumor cerebral microvessels following RT in C57Bl6J mice, offering key insights into the impact of radiation on vascular health. A total of 414 dysregulated proteins were identified, with 257 showing downregulation. These findings highlight mitochondrial dysfunction and metabolic disruptions as central themes, with notable effects on pathways such as oxidative phosphorylation, the TCA cycle, and glycolysis.

Pathway enrichment analysis revealed significant alterations in 266 pathways. Among 76 canonical pathways, 68 were inhibited (e.g., oxidative phosphorylation), while 8 were activated (e.g., mitochondrial dysfunction). Mitochondrial proteins were particularly impacted, with a detailed analysis identifying 84 downregulated proteins linked to the mitochondrial inner membrane and respiratory chain complex I, indicating disrupted energy metabolism.

Proteomic changes also revealed inhibition of ATP synthesis, cell migration, and other cellular processes through pathways such as nucleo-cytosolic transport and spliceosomal activity. Increased oxidative stress was evidenced by the activation of reactive oxygen species synthesis, potentially as a result of mitochondrial dysfunction. Enriched disease-related processes further pointed to disruptions in molecule transport and fatty acid metabolism. Western blot analysis of OXPHOS proteins confirmed inhibited energy metabolism and mitochondrial dysfunction. These findings underscore the lasting effects of RT caused by RT in cerebral microvessels, particularly on mitochondrial health and metabolic pathways.

Given the strong impact of RT on the mitochondrial proteome, our study focused on changes in the mitochondrial and metabolic proteome. In most vascular beds, endothelial cells (ECs) predominantly

16

use glycolysis and depend minimally on mitochondrial OXPHOS for ATP generation, as mitochondrial volume in ECs constitutes only 2–6% of total cellular volume [43,44]. However, cerebromicrovascular ECs at the BBB possess nearly double the mitochondrial volume compared to other vascular beds [45]. The BBB represents a selective yet dynamic interface between the blood and central nervous system that rigorously maintains neuronal homeostasis by regulating the transport of substances to and from the brain [46,47]. The cerebral microvasculature engages in aerobic respiration to support the energy demands required for maintaining transport systems and barrier function [48]. Doll and colleagues reported that mitochondrial "crisis" induced by a lipopolysaccharide challenge in cerebromicrovascular ECs significantly compromises BBB function in vitro and in vivo [47] but similar data after RT have been missing so far.

Since glycolysis is the primary metabolic pathway for energy production in ECs, it remains to be established how the extensive alterations in metabolic function following RT affect EC phenotypes. As such, further studies are needed to explore the positive link between energy depletion and EC dysfunction, for example, whether energy deficiency drives or results from long-term changes post-RT, including altered BBB permeability, cellular senescence, impaired angiogenesis, increased inflammation, reduced nitric oxide production, and a pro-thrombotic state [43,49-53]. Since these changes may contribute to complications like neuroinflammation and ischemia in irradiated areas, largely due to the disruption of vascular homeostasis, targeting metabolic pathways may offer a novel approach to mitigating these long-term side effects.

Beyond metabolism, mitochondrial signaling is gaining recognition for its role in RT-induced tissue injury [54-57]. While mitochondrial reactive oxygen species (ROS) have been highlighted as mediators of mitochondrial DNA damage and ETC dysfunction in ECs, additional factors, such as altered mitochondrial calcium in- and efflux, may also contribute [22,56,58,59]. Moreover, mitochondrial DNA

fragments as damage-associated molecular patterns may drive inflammatory signaling cascades after RT [60].

Additional to changes in the mitochondrial and metabolic proteome, our findings highlight dysregulation in proteins related to mRNA splicing and stress-response pathways, suggesting that RT drives transcriptional and post-transcriptional modifications [61]. These changes potentially disrupt cellular homeostasis and protein synthesis, aggravating vascular dysfunction and warrant further investigation.

This study has several limitations. Firstly, exclusively male mice were used. Given merging evidence for differences in radiosensitivity in males versus females, findings should be validated in female mice [62]. Secondly, the contributions of different cell types, such as pericytes, astrocytes, and ECs, cannot be fully resolved with the current methods. Thirdly, observations were limited to a single time point; future studies should examine various time points to provide a more comprehensive understanding of changes over time. Lastly, additional mechanistic studies are needed to confirm proteome study predictions about EC phenotypes, including respiration, barrier dysfunction, and mRNA processing.

In conclusion, our study provides evidence for mitochondrial dysfunction and dysregulation of protein synthesis pathways in cerebromicrovascular ECs following RT. These findings shed light on potential mechanisms underlying radiation-induced BBB breakdown and highlight the need for further investigation into the role of mitochondria in ECs. They also underscore the need for further research into the relationship between mitochondrial integrity, metabolic function, and vascular health in RT contexts.

Conflict of Interest statement

None of the authors indicated a conflict of interest.

Funding statement

REFERENCES

1. Dimitrievich GS, Hausladen SL, Kuchnir FT, Griem ML. Radiation damage and subendothelial repair to rabbit ear chamber microvasculature. An in vivo and histologic study. *Radiat Res*. 1977;69:276-292.

2. Adamson IY, Bowden DH. Endothelial injury and repair in radiation-induced pulmonary fibrosis. *Am J Pathol*. 1983;112:224-230.

3. Narayan K, Cliff WJ. Morphology of irradiated microvasculature: a combined in vivo and electron-microscopic study. *Am J Pathol*. 1982;106:47-62.

4. Baselet B, Sonveaux P, Baatout S, Aerts A. Pathological effects of ionizing radiation: endothelial activation and dysfunction. *Cell Mol Life Sci*. 2019;76:699-728. doi: 10.1007/s00018-018-2956-z

5. Hatoum OA, Otterson MF, Kopelman D, Miura H, Sukhotnik I, Larsen BT, Selle RM, Moulder JE, Gutterman DD. Radiation induces endothelial dysfunction in murine intestinal arterioles via enhanced production of reactive oxygen species. *Arterioscler Thromb Vasc Biol*. 2006;26:287-294. doi: 10.1161/01.ATV.0000198399.40584.8c

6. Coderre JA, Morris GM, Micca PL, Hopewell JW, Verhagen I, Kleiboer BJ, van der Kogel AJ. Late effects of radiation on the central nervous system: role of vascular endothelial damage and glial stem cell survival. *Radiat Res*. 2006;166:495-503. doi: 10.1667/RR3597.1

7. Lyubimova N, Hopewell JW. Experimental evidence to support the hypothesis that damage to vascular endothelium plays the primary role in the development of late radiation-induced CNS injury. *Br J Radiol*. 2004;77:488-492. doi: 10.1259/bjr/15169876

8. Li YQ, Chen P, Haimovitz-Friedman A, Reilly RM, Wong CS. Endothelial apoptosis initiates acute blood-brain barrier disruption after ionizing radiation. *Cancer Res*. 2003;63:5950-5956.

9. Greene-Schloesser D, Moore E, Robbins ME. Molecular pathways: radiation-induced cognitive impairment. *Clin Cancer Res*. 2013;19:2294-2300. doi: 10.1158/1078-0432.CCR-11-2903

10. Drayson OGG, Vozenin MC, Limoli CL. A rigorous behavioral testing platform for the assessment of radiation-induced neurological outcomes. *Methods Cell Biol*. 2023;180:177-197. doi: 10.1016/bs.mcb.2023.02.015

11. Lehrer EJ, Jones BM, Dickstein DR, Green S, Germano IM, Palmer JD, Laack N, Brown PD, Gondi V, Wefel JS, et al. The Cognitive Effects of Radiotherapy for Brain Metastases. *Front Oncol*. 2022;12:893264. doi: 10.3389/fonc.2022.893264

12. Tsang DS, Khandwala MM, Liu ZA, Richard N, Shen G, Sekely A, Bernstein LJ, Simpson R, Mason W, Chung C, et al. Neurocognitive Performance in Adults Treated With Radiation for a Primary Brain Tumor. *Adv Radiat Oncol*. 2022;7:101028. doi: 10.1016/j.adro.2022.101028

13. Cramer CK, Cummings TL, Andrews RN, Strowd R, Rapp SR, Shaw EG, Chan MD, Lesser GJ. Treatment of Radiation-Induced Cognitive Decline in Adult Brain Tumor Patients. *Curr Treat Options Oncol*. 2019;20:42. doi: 10.1007/s11864-019-0641-6

14. Cramer CK, McKee N, Case LD, Chan MD, Cummings TL, Lesser GJ, Shaw EG, Rapp SR. Mild cognitive impairment in long-term brain tumor survivors following brain irradiation. *J Neurooncol*. 2019;141:235-244. doi: 10.1007/s11060-018-03032-8

15. Haldbo-Classen L, Amidi A, Wu LM, Lukacova S, Oettingen GV, Gottrup H, Zachariae R, Høyer M. Long-term cognitive dysfunction after radiation therapy for primary brain tumors. *Acta Oncol*. 2019;58:745-752. doi: 10.1080/0284186X.2018.1557786

16. Makale MT, McDonald CR, Hattangadi-Gluth JA, Kesari S. Mechanisms of radiotherapy-associated cognitive disability in patients with brain tumours. *Nat Rev Neurol*. 2017;13:52-64. doi: 10.1038/nrneurol.2016.185

17. Nordal RA, Wong CS. Molecular targets in radiation-induced blood-brain barrier disruption. *Int J Radiat Oncol Biol Phys*. 2005;62:279-287. doi: 10.1016/j.ijrobp.2005.01.039

18. Ungvari Z, Podlutsky A, Sosnowska D, Tucsek Z, Toth P, Deak F, Gautam T, Csiszar A, Sonntag WE. Ionizing radiation promotes the acquisition of a senescence-associated secretory phenotype and impairs angiogenic capacity in cerebromicrovascular endothelial cells: role of

increased DNA damage and decreased DNA repair capacity in microvascular radiosensitivity. *J Gerontol A Biol Sci Med Sci*. 2013;68:1443-1457. doi: 10.1093/gerona/glt057

19. Buszek SM, Al Feghali KA, Elhalawani H, Chevli N, Allen PK, Chung C. Optimal Timing of Radiotherapy Following Gross Total or Subtotal Resection of Glioblastoma: A Real-World Assessment using the National Cancer Database. *Sci Rep*. 2020;10:4926. doi: 10.1038/s41598-020-61701-z

20. Johannesen TB, Lien HH, Hole KH, Lote K. Radiological and clinical assessment of long-term brain tumour survivors after radiotherapy. *Radiother Oncol*. 2003;69:169-176. doi: 10.1016/s0167-8140(03)00192-0

21. Ait-Aissa K, Guo X, Klemmensen M, Leng LN, Koval OM, Grumbach IM. Short-term statin treatment reduces, and long-term statin treatment abolishes chronic vascular injury by radiation therapy. *bioRxiv*. 2023. doi: 10.1101/2023.09.20.558723

22. Ait-Aissa K, Koval OM, Lindsey NR, Grumbach IM. Mitochondrial Ca. *Arterioscler Thromb Vasc Biol*. 2022;42:1121-1136. doi: 10.1161/ATVBAHA.122.317869

23. Murley JS, Kataoka Y, Weydert CJ, Oberley LW, Grdina DJ. Delayed radioprotection by nuclear transcription factor kappaB -mediated induction of manganese superoxide dismutase in human microvascular endothelial cells after exposure to the free radical scavenger WR1065. *Free Radic Biol Med*. 2006;40:1004-1016. doi: 10.1016/j.freeradbiomed.2005.10.060

24. Hu S, Gao Y, Zhou H, Kong F, Xiao F, Zhou P, Chen Y. New insight into mitochondrial changes in vascular endothelial cells irradiated by gamma ray. *Int J Radiat Biol*. 2017;93:470-476. doi: 10.1080/09553002.2017.1286048

25. Kouam PN, Rezniczek GA, Adamietz IA, Bühler H. Ionizing radiation increases the endothelial permeability and the transendothelial migration of tumor cells through ADAM10-activation and subsequent degradation of VE-cadherin. *BMC Cancer*. 2019;19:958. doi: 10.1186/s12885-019-6219-7

26. Lee YK, Uchida H, Smith H, Ito A, Sanchez T. The isolation and molecular characterization of cerebral microvessels. *Nat Protoc*. 2019;14:3059-3081. doi: 10.1038/s41596-019-0212-0

27. Hughes CS, Foehr S, Garfield DA, Furlong EE, Steinmetz LM, Krijgsveld J. Ultrasensitive proteome analysis using paramagnetic bead technology. *Mol Syst Biol*. 2014;10:757. doi: 10.15252/msb.20145625

28. Cox J, Mann M. MaxQuant enables high peptide identification rates, individualized p.p.b.-range mass accuracies and proteome-wide protein quantification. *Nat Biotechnol*. 2008;26:1367-1372. doi: 10.1038/nbt.1511

29. Cox J, Hein MY, Luber CA, Paron I, Nagaraj N, Mann M. Accurate proteome-wide label-free quantification by delayed normalization and maximal peptide ratio extraction, termed MaxLFQ. *Mol Cell Proteomics*. 2014;13:2513-2526. doi: 10.1074/mcp.M113.031591

30. Vizcaíno JA, Côté RG, Csordas A, Dianes JA, Fabregat A, Foster JM, Griss J, Alpi E, Birim M, Contell J, et al. The PRoteomics IDEntifications (PRIDE) database and associated tools: status in 2013. *Nucleic Acids Res*. 2013;41:D1063-1069. doi: 10.1093/nar/gks1262

31. Azimzadeh O, Subramanian V, Sievert W, Merl-Pham J, Oleksenko K, Rosemann M, Multhoff G, Atkinson MJ, Tapio S. Activation of PPARα by Fenofibrate Attenuates the Effect of Local Heart High Dose Irradiation on the Mouse Cardiac Proteome. *Biomedicines*. 2021;9. doi: 10.3390/biomedicines9121845

32. Philipp J, Sievert W, Azimzadeh O, von Toerne C, Metzger F, Posch A, Hladik D, Subedi P, Multhoff G, Atkinson MJ, et al. Data independent acquisition mass spectrometry of irradiated mouse lung endothelial cells reveals a STAT-associated inflammatory response. *Int J Radiat Biol*. 2020;96:642-650. doi: 10.1080/09553002.2020.1712492

33. Subramanian V, Borchard S, Azimzadeh O, Sievert W, Merl-Pham J, Mancuso M, Pasquali E, Multhoff G, Popper B, Zischka H, et al. PPARα Is Necessary for Radiation-Induced Activation of Noncanonical TGFβ Signaling in the Heart. *J Proteome Res*. 2018;17:1677-1689. doi: 10.1021/acs.jproteome.8b00001

34. Tang D, Chen M, Huang X, Zhang G, Zeng L, Zhang G, Wu S, Wang Y. SRplot: A free online platform for data visualization and graphing. *PLoS One*. 2023;18:e0294236. doi: 10.1371/journal.pone.0294236

35. Goedhart J, Luijsterburg MS. VolcaNoseR is a web app for creating, exploring, labeling and sharing volcano plots. *Sci Rep*. 2020;10:20560. doi: 10.1038/s41598-020-76603-3

36. Ning W, Wei Y, Gao L, Han C, Gou Y, Fu S, Liu D, Zhang C, Huang X, Wu S, et al. HemI 2.0: an online service for heatmap illustration. *Nucleic Acids Res*. 2022;50:W405-w411. doi: 10.1093/nar/gkac480

37. Krämer A, Green J, Pollard J, Jr., Tugendreich S. Causal analysis approaches in Ingenuity Pathway Analysis. *Bioinformatics*. 2014;30:523-530. doi: 10.1093/bioinformatics/btt703

38. Ahsan S, Drăghici S. Identifying Significantly Impacted Pathways and Putative Mechanisms with iPathwayGuide. *Curr Protoc Bioinformatics*. 2017;57:7.15.11-17.15.30. doi: 10.1002/cpbi.24

39. Azimzadeh O, Azizova T, Merl-Pham J, Subramanian V, Bakshi MV, Moseeva M, Zubkova O, Hauck SM, Anastasov N, Atkinson MJ, et al. A dose-dependent perturbation in cardiac energy metabolism is linked to radiation-induced ischemic heart disease in Mayak nuclear workers. *Oncotarget*. 2017;8:9067-9078. doi: 10.18632/oncotarget.10424

40. Barjaktarovic Z, Shyla A, Azimzadeh O, Schulz S, Haagen J, Dörr W, Sarioglu H, Atkinson MJ, Zischka H, Tapio S. Ionising radiation induces persistent alterations in the cardiac mitochondrial function of C57BL/6 mice 40 weeks after local heart exposure. *Radiother Oncol*. 2013;106:404-410. doi: 10.1016/j.radonc.2013.01.017

41. Buss LG, Rheinheimer BA, Limesand KH. Radiation-induced changes in energy metabolism result in mitochondrial dysfunction in salivary glands. *Sci Rep*. 2024;14:845. doi: 10.1038/s41598-023-50877-9

42. Pierre-Louis Odoom J, Freeberg MAT, Camus SV, Toft R, Szomju BB, Sanchez Rosado RM, Jackson PD, Allegood JC, Silvey S, Liu J, et al. Exhaled breath condensate identifies metabolic dysregulation in patients with radiation-induced lung injury. *Am J Physiol Lung Cell Mol Physiol*. 2023;324:L863-l869. doi: 10.1152/ajplung.00439.2022

43. Eelen G, de Zeeuw P, Simons M, Carmeliet P. Endothelial cell metabolism in normal and diseased vasculature. *Circ Res*. 2015;116:1231-1244. doi: 10.1161/CIRCRESAHA.116.302855

44. Tang X, Luo YX, Chen HZ, Liu DP. Mitochondria, endothelial cell function, and vascular diseases. *Front Physiol*. 2014;5:175. doi: 10.3389/fphys.2014.00175

45. Oldendorf WH, Cornford ME, Brown WJ. The large apparent work capability of the blood-brain barrier: a study of the mitochondrial content of capillary endothelial cells in brain and other tissues of the rat. *Ann Neurol*. 1977;1:409-417. doi: 10.1002/ana.410010502

46. Bukeirat M, Sarkar SN, Hu H, Quintana DD, Simpkins JW, Ren X. MiR-34a regulates blood-brain barrier permeability and mitochondrial function by targeting cytochrome c. *J Cereb Blood Flow Metab*. 2016;36:387-392. doi: 10.1177/0271678X15606147

47. Doll DN, Hu H, Sun J, Lewis SE, Simpkins JW, Ren X. Mitochondrial crisis in cerebrovascular endothelial cells opens the blood-brain barrier. *Stroke*. 2015;46:1681-1689. doi: 10.1161/strokeaha.115.009099

48. Sakamuri SS, Sure VN, Kolli L, Evans WR, Sperling JA, Bix GJ, Wang X, Atochin DN, Murfee WL, Mostany R, et al. Aging related impairment of brain microvascular bioenergetics involves oxidative phosphorylation and glycolytic pathways. *J Cereb Blood Flow Metab*. 2022;42:1410-1424. doi: 10.1177/0271678X211069266

49. Bierhansl L, Conradi LC, Treps L, Dewerchin M, Carmeliet P. Central Role of Metabolism in Endothelial Cell Function and Vascular Disease. *Physiology (Bethesda)*. 2017;32:126-140. doi: 10.1152/physiol.00031.2016

50. Erusalimsky JD. Vascular endothelial senescence: from mechanisms to pathophysiology. *J Appl Physiol (1985)*. 2009;106:326-332. doi: 10.1152/japplphysiol.91353.2008

51. Sabbatinelli J, Prattichizzo F, Olivieri F, Procopio AD, Rippo MR, Giuliani A. Where Metabolism Meets Senescence: Focus on Endothelial Cells. *Front Physiol*. 2019;10:1523. doi: 10.3389/fphys.2019.01523

52. Kim ES, Kim KS, Lee CH, Jeon MT, Lee SB, Lee JH, Kim DG. Brain Endothelial Cells Utilize Glycolysis for the Maintenance of the Transcellular Permeability. *Mol Neurobiol*. 2022;59:4315-4333. doi: 10.1007/s12035-022-02778-7

53. Leung SWS, Shi Y. The glycolytic process in endothelial cells and its implications. *Acta Pharmacol Sin*. 2022;43:251-259. doi: 10.1038/s41401-021-00647-y

54. Parihar VK, Allen BD, Tran KK, Chmielewski NN, Craver BM, Martirosian V, Morganti JM, Rosi S, Vlkolinsky R, Acharya MM, et al. Targeted overexpression of mitochondrial catalase prevents radiation-induced cognitive dysfunction. *Antioxid Redox Signal*. 2015;22:78-91. doi: 10.1089/ars.2014.5929

55. Baselet B, Driesen RB, Coninx E, Belmans N, Sieprath T, Lambrichts I, De Vos WH, Baatout S, Sonveaux P, Aerts A. Rosiglitazone Protects Endothelial Cells From Irradiation-Induced Mitochondrial Dysfunction. *Front Pharmacol*. 2020;11:268. doi: 10.3389/fphar.2020.00268

56. Livingston K, Schlaak RA, Puckett LL, Bergom C. The Role of Mitochondrial Dysfunction in Radiation-Induced Heart Disease: From Bench to Bedside. *Front Cardiovasc Med*. 2020;7:20. doi: 10.3389/fcvm.2020.00020

57. Yamamori T, Ike S, Bo T, Sasagawa T, Sakai Y, Suzuki M, Yamamoto K, Nagane M, Yasui H, Inanami O. Inhibition of the mitochondrial fission protein dynamin-related protein 1 (Drp1) impairs mitochondrial fission and mitotic catastrophe after x-irradiation. *Mol Biol Cell*. 2015;26:4607-4617. doi: 10.1091/mbc.E15-03-0181

58. Lafargue A, Degorre C, Corre I, Alves-Guerra MC, Gaugler MH, Vallette F, Pecqueur C, Paris F. Ionizing radiation induces long-term senescence in endothelial cells through mitochondrial respiratory complex II dysfunction and superoxide generation. *Free Radic Biol Med*. 2017;108:750-759. doi: 10.1016/j.freeradbiomed.2017.04.019

59. Szumiel I. Ionizing radiation-induced oxidative stress, epigenetic changes and genomic instability: the pivotal role of mitochondria. *Int J Radiat Biol*. 2015;91:1-12. doi: 10.3109/09553002.2014.934929

60. Averbeck D, Rodriguez-Lafrasse C. Role of Mitochondria in Radiation Responses: Epigenetic, Metabolic, and Signaling Impacts. *Int J Mol Sci*. 2021;22. doi: 10.3390/ijms222011047

61. Macaeva E, Saeys Y, Tabury K, Janssen A, Michaux A, Benotmane MA, De Vos WH, Baatout S, Quintens R. Radiation-induced alternative transcription and splicing events and their applicability to practical biodosimetry. *Sci Rep*. 2016;6:19251. doi: 10.1038/srep19251

62. Taliaferro LP, Agarwal RK, Coleman CN, DiCarlo AL, Hofmeyer KA, Loelius SG, Molinar-Inglis O, Tedesco DC, Satyamitra MM. Sex differences in radiation research. *Int J Radiat Biol*. 2024;100:466-485. doi: 10.1080/09553002.2023.2283089
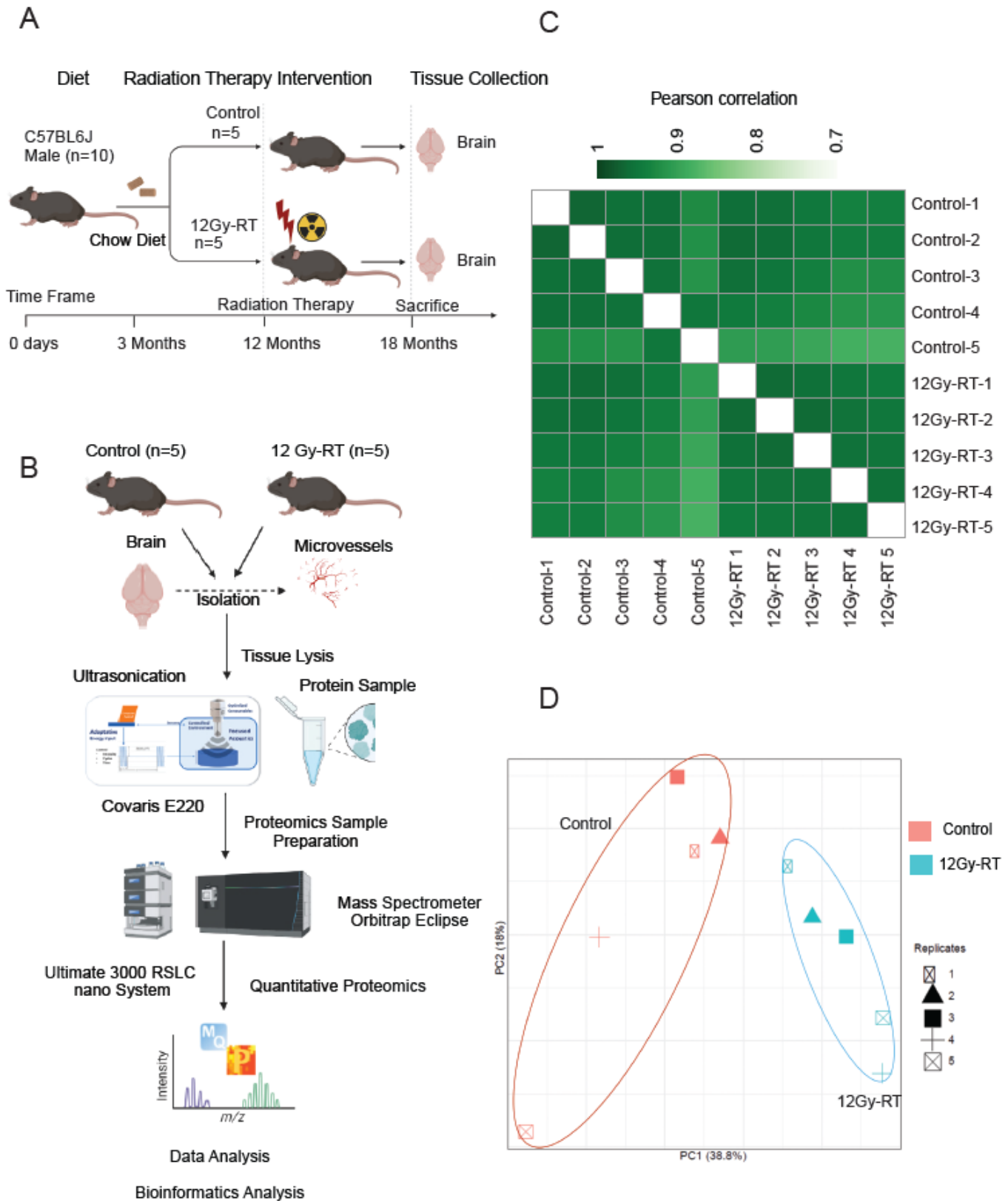
Figure 1

Figure 1: Quantitative proteomics analysis of the cerebral microvessels. **(A)** Workflow for radiation therapy (RT) and sample collection. **(B)** Workflow for high-throughput identification and quantification of proteins from cerebral microvessels in control and irradiated mice (12 Gy-RT). **(C)** Pearson correlation matrix based on label-free quantification (LFQ) intensities, showing sample reproducibility in control and irradiated groups. **(D)** Principal component analysis (PCA) plot for proteins identified in biological replicates of control and irradiated groups.

Figure 2
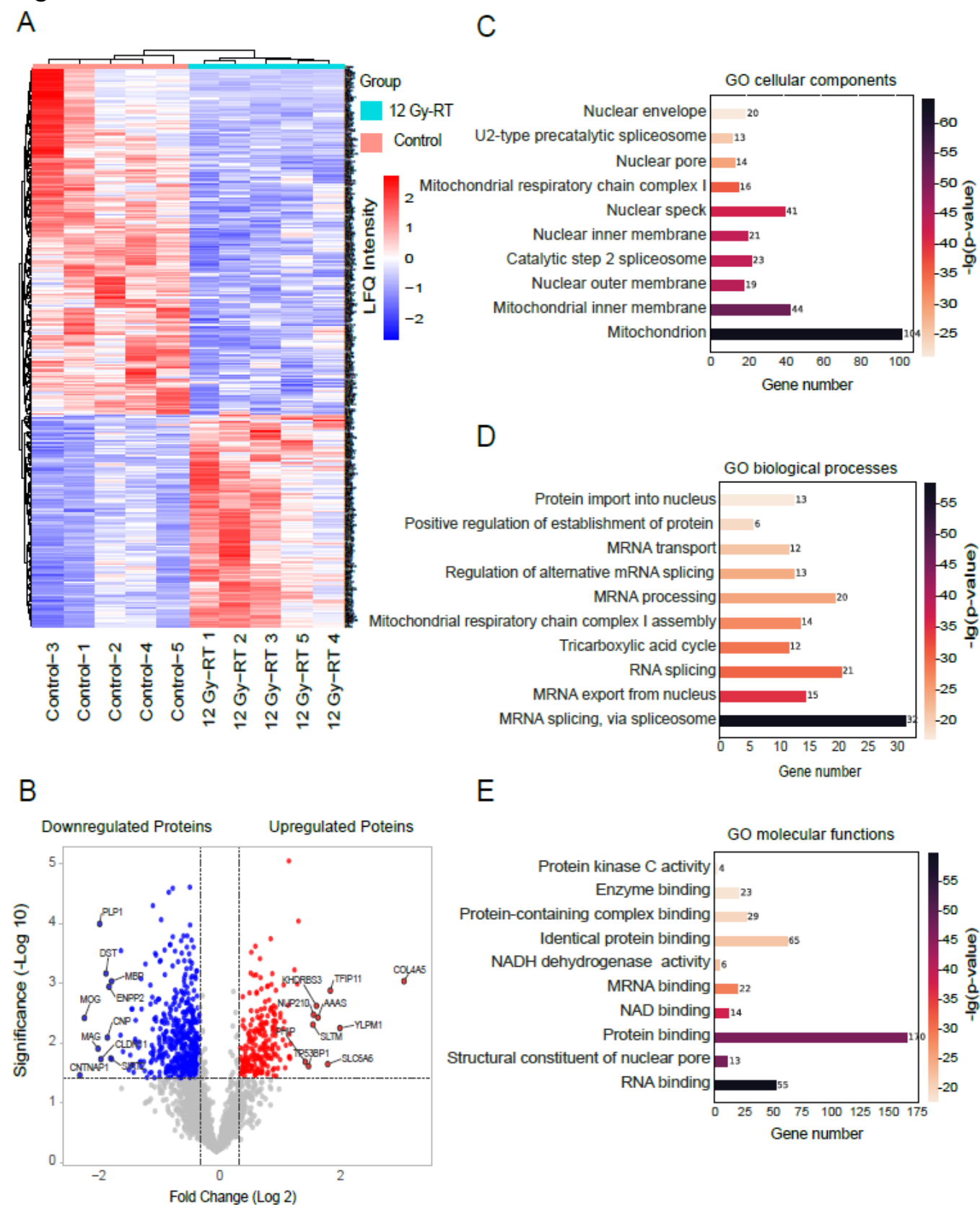
Figure 2: Significant differences in the cerebral microvessel proteomes between control and irradiated groups. **(A)** Hierarchical clustering analysis (heatmap) using unsupervised Euclidean distance for differentially expressed proteins across biological replicates. Z-scored LFQ intensities for individual mice are shown side by side. **(B)** Volcano plots of differentially expressed proteins, with the y-axis representing −log10 p-value significance and the x-axis representing log2 fold change. The top 10 proteins with the most significant decrease and increase in expression are highlighted in blue and red, respectively (p < 0.05). The dotted line indicates the cut-off for protein expression fold change (log2) against statistical significance [-log10 (p-value)]. **(C)** GO cellular components, **(D)** GO biological processes, and **(E)** GO molecular function analysis of significantly dysregulated proteins compared to the control group. The top 10 enriched GO terms are displayed with corrected p-values and gene numbers. The colored bar indicates enriched terms with corresponding corrected p-values and gene numbers. Analyses were performed using the HemI 2.0 web tool.
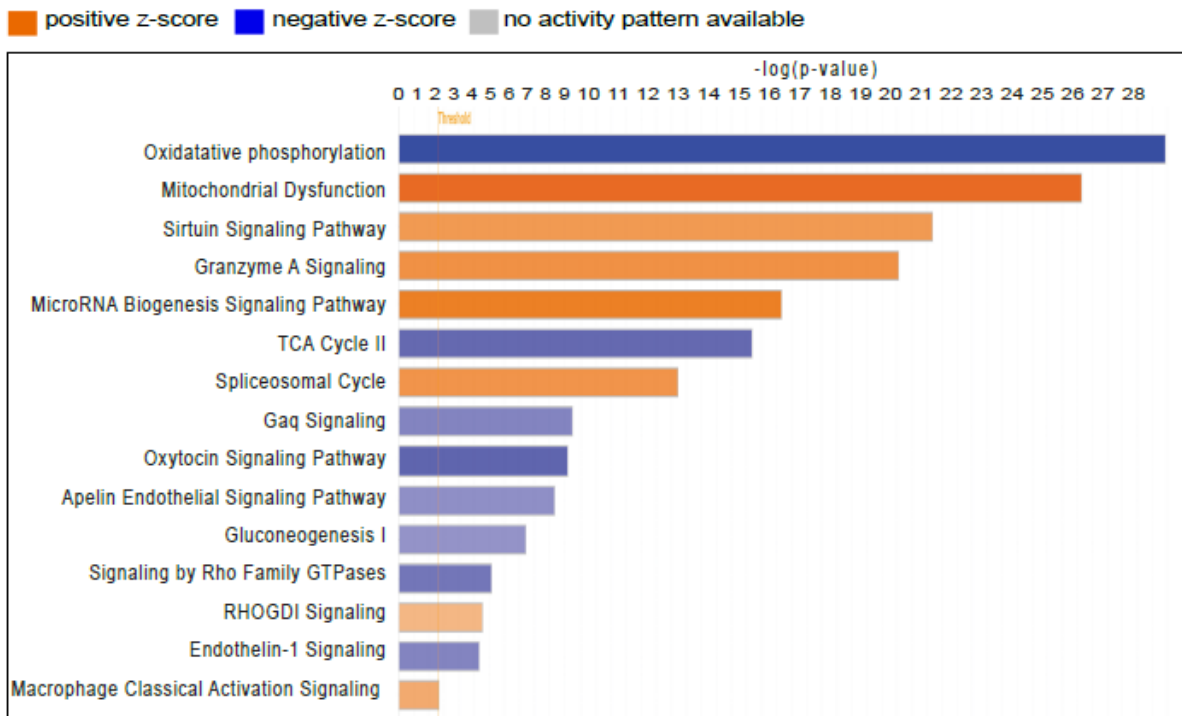
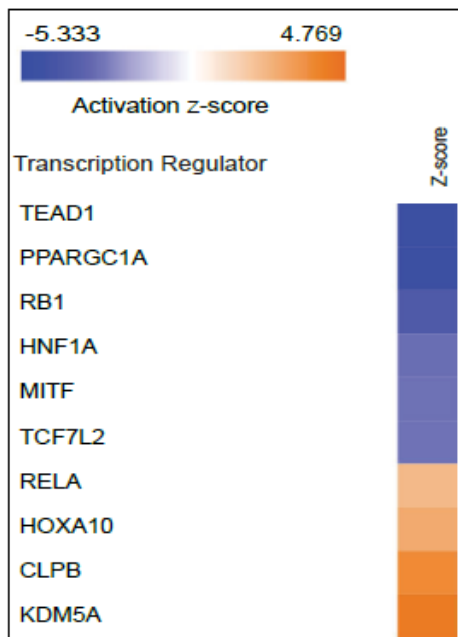# Figure 3
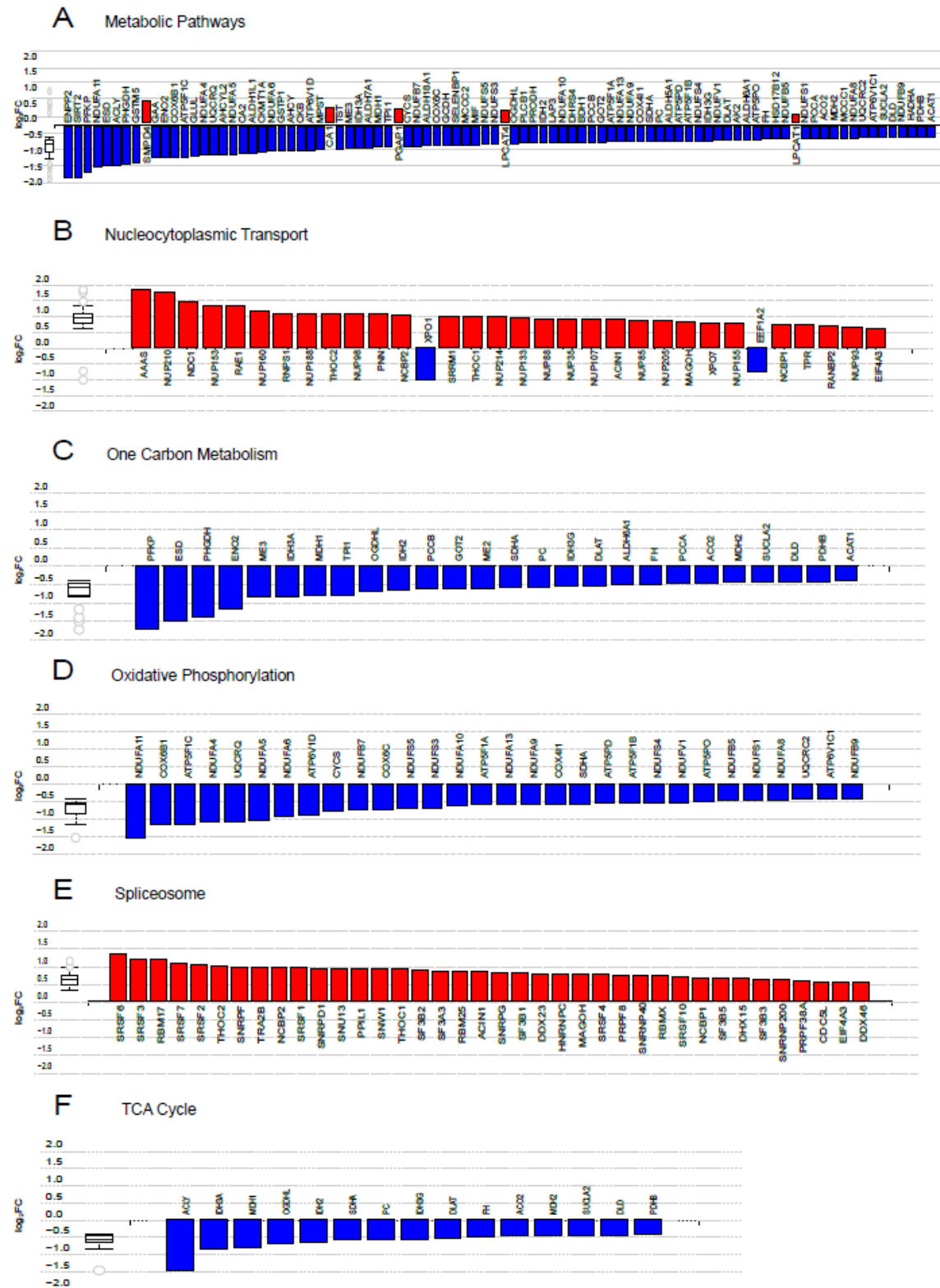
(c) Advaita Corporation 2023

Figure 3: Impact pathway (iPathway guide) analysis of dysregulated proteins by RT. (A-F) Bar graphs showing dysregulated proteins mapped to pathways identified by iPathway analysis based on FDR-corrected p-value significance: **(A)** Metabolic pathways, **(B)** nucleocytoplasmic transport, **(C)** one carbon metabolism, **(D)** oxidative phosphorylation**, (E)** spliceosome, and **(F)** TCA cycle. Genes are ranked by absolute log-fold change, with upregulated genes in red and downregulated genes in blue. Box-and-whisker plots summarize the distribution of differentially expressed genes in each pathway, with boxes representing the 1st quartile, median, and 3rd quartile, and circles indicating outliers.
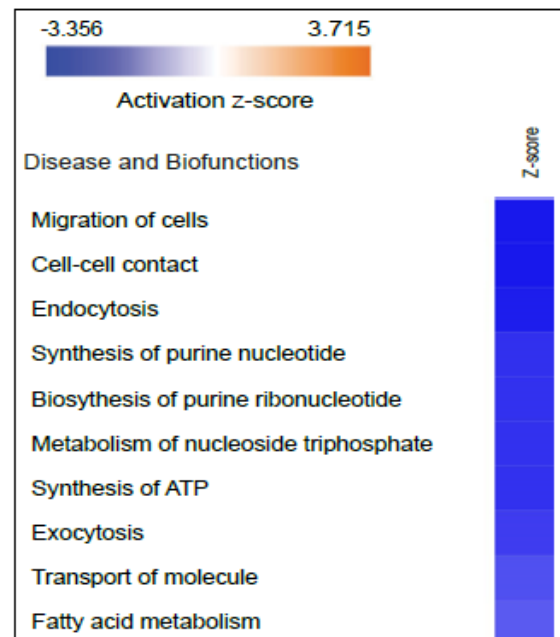
Figure 4

Figure 4: Ingenuity pathway analysis (IPA) of all dysregulated proteins from the irradiated group. **(A)** Fifteen selected canonical pathways predicted to be activated or inhibited based on z-scores and a B–H p-value < 0.05 (calculated using Fisher's exact test and adjusted with the Benjamini-Hochberg method). A positive z-score (orange) indicates pathway activation, while a negative z-score (blue) indicates inhibition. Longer bars indicate stronger significance (source: http://www.INGENUITY.com). **(B)** Heatmap of the top 10 transcription regulators predicted to be activated (z-scores > 2) or inhibited (z-scores < -2). **(C)** Predicted activation or inhibition of selected diseases and biofunctions based on z-scores (> 2 for activation; < -2 for inhibition) in the irradiated group.
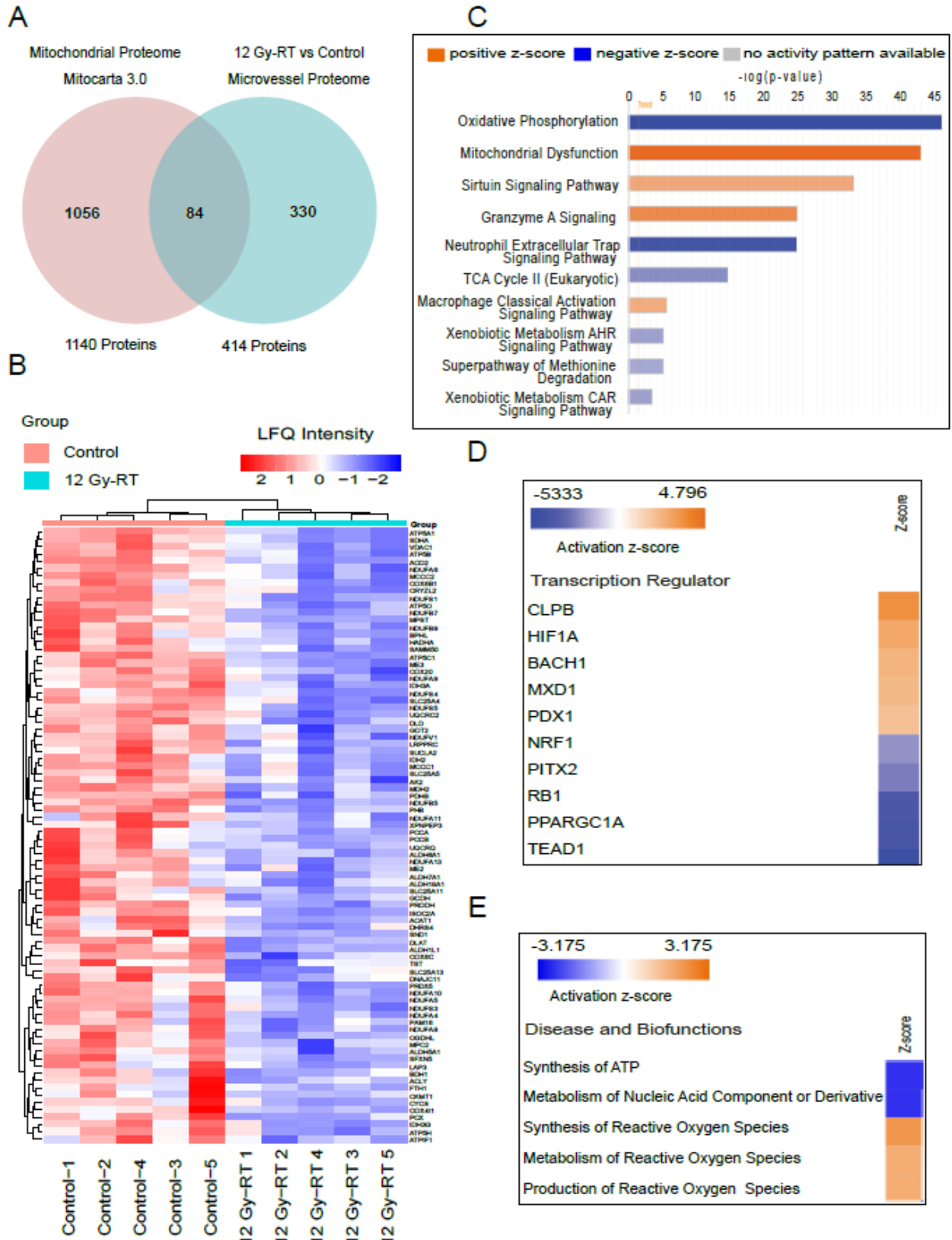
Figure 5

Figure 5: Ingenuity pathway analysis (IPA) of mitochondrial proteins that are dysregulated in the irradiated group. (A) Venn diagram showing 84 mitochondrial proteins shared between the mitochondrial proteome database (Mitocarta 3.0) and the cerebral microvessel proteome. **(B)** Hierarchical clustering analysis (heatmap) of differentially expressed mitochondrial proteins across biological replicates from control and irradiated groups, with z-scored LFQ intensities for individual mice. **(C)** Top 10 predicted canonical pathways based on z-scores and B–H p-values < 0.05 (calculated using Fisher's exact test and adjusted with the Benjamini-Hochberg method). A positive z-score (orange) indicates pathway activation, while a negative z-score (blue) indicates inhibition (source: http://www.INGENUITY.com). **(D)** Heatmap of the top 10 transcription regulators predicted to be activated (z-scores > 2) or inhibited (z-scores < -2). **(E)** Predicted activation or inhibition of selected diseases and biofunctions based on z-scores (> 2 for activation; < -2 for inhibition) in the irradiated group.
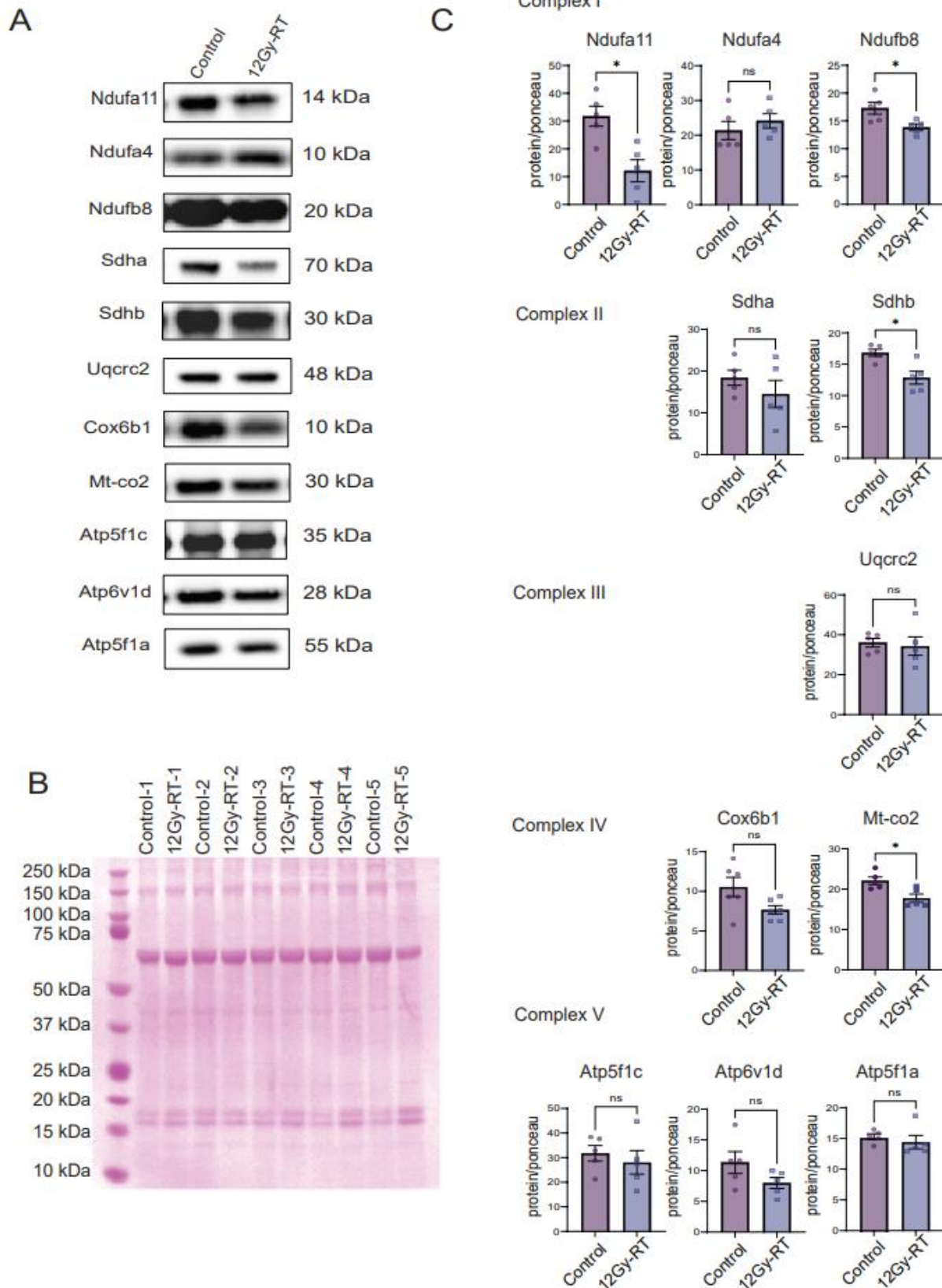
Figure 6

Figure 6: Validation of Metabolic Protein Expression Changes by Immunoblot
(A) Representative immunoblot images for OXPHOS complex subunits in control and irradiated groups. **(B)** Ponceau-stained membrane used as loading control. **(C)** Immunoblots of ETC complex I proteins (NDUFA11, NDUFA4, NDUFB8), complex II proteins (SDHA, SDHB), complex III protein (UQCRC2), complex IV proteins (COX6B1, MT-CO2), and complex V proteins (ATP5F1C, ATP6VID, ATP5F1A) in control and irradiated groups. Quantification of protein levels after normalization to Ponceau-stained membrane. Analysis by Mann-Whitney test.